Supporting Information

Probing Intersystem Crossing in Multi-brominated Eumelanin through Transient Absorption and Surface Hopping Dynamics

Kavya Vinod[†a], Lukhmanul Hakeem K.[†a], Diana Thomas[a], Pallavi Panthakkal Das[a] and Mahesh Hariharan*[a]

[a]School of Chemistry, Indian Institute of Science Education and Research Thiruvananthapuram, Vithura, Thiruvananthapuram, Kerala, India 695551

Table of Contents

Section 4: Figures

Section 1: Materials and Methods

All reagents, except N-bromosuccinimide and DMICE, were used as supplied by the commercial vendors. N-bromosuccinimide, obtained from TCI India, was recrystallized from water, while DMICE, sourced from BLDPharm India, was purified by column chromatography using a dichloromethane/hexane mixture before use. All the reactions were carried out in oven-dried glassware before use. Standard gastight syringes and septa were used in the process. Standard purification techniques for drying and distillation were used for all the solvents involved in characterization. Column chromatography was performed using silica gel (80-200 mesh). Yields correspond to spectroscopically pure substances. High-resolution mass spectra (HRMS) were obtained using a Thermo Scientific Q mass spectrometer. ^{1}H and ^{13}C NMR spectra were measured on a 500 MHz Bruker Advance DPX spectrometer using 1,1,1,1-tetramethyl silane (TMS) as the internal standard. Steady-state photophysical measurements were carried out in a cuvette of 1 cm path length. Absorption and spectra were recorded on a Shimadzu UV-3600 UV-VIS-NIR spectrometer and emission and phosphorescence spectra were recorded in Horiba Jobin Yvon Fluorolog spectrometer. The pulse-width of the flash lamp for phosphorescence measurement is 3 µs. The UV-vis absorption spectra in the solution state were measured using the transmission mode and the Kubelka-Munk transformed reflectance spectra in the crystalline state were recorded using diffuse reflectance mode. The crystals were placed on a $BaSO_4$-coated plate for the Kubelka-Munk experiments. The samples were then pressed into the sample holder of the integrated sphere accessory of the Shimadzu UV-3600 UV-vis-NIR spectrophotometer and the diffuse reflectance spectra were recorded.

1.1 X-ray Crystallography

High quality single crystals of DMICE-Br_2 and DMICE-Br_3 were utilized for X-ray diffraction experiments. The crystals were mounted on a glass fiber using Infineum V8512 oil. All measurements were made on a CCD area detector with graphite monochromated Mo Kα radiation. The data was collected using Bruker APEXII detector and processed using APEX2 from Bruker. The structure was solved by direct method and expanded using Fourier technique. The non-hydrogen atoms were refined anisotropically. Hydrogen atoms were included in idealized positions, but not refined. The structure was refined using Olex2 software. The full validation of CIF and structure factor of DMICE-Br_2 and DMICE-Br_3 were performed using the checkCIF utility and found to be free of major alert levels. Three-dimensional structure visualization and the exploration of the crystal packing of crystals under study were carried out using Mercury 2021.2.0.[64]

1.2 Computational Details

1.2a The linear vibronic coupling model[1, 2]

We utilized the LVC model to construct the excited state potential energy surfaces (PESs) of both DMICE-Br_2 and DMICE-Br_3, which were then used for trajectory surface hopping simulation. The LVC model employed within SHARC was parametrized in accordance with the methodology outlined in the relevant literature.[1] Here we describe a very brief overview of the reported method. LVC model describes the excited state PESs V in terms of ground state potential V_0 and state-specific vibronic coupling term W.

$$\boldsymbol{V} = \boldsymbol{V_0}\mathbf{1} + \boldsymbol{W} \qquad \text{(Equation S1)}$$

Where ground state potential is defined in terms of harmonic approximation by the following equation:

$$\boldsymbol{V_0} = \frac{\mathbf{1}}{\mathbf{2}}\,\boldsymbol{r^T H_0} \qquad \text{(Equation S2)}$$

Where r denotes the displacement from the reference geometry in Cartesian coordinates and H_0 is the ground state Hessian. To rewrite this equation, one first diagonalizes mass-weighted hessian and finally, the equation was written in terms of mass-frequency-weighted normal mode coordinate Q_i and normal-mode frequencies ω_i

$$V_0 = \sum_i \frac{\hbar\omega_i}{2}\, Q_i^2 \qquad \text{(Equation S3)}$$

Where Qi is defined by the following equation

$$\mathrm{Qi} = \sqrt{\frac{\omega_i}{\hbar}} \sum_\alpha K_{\alpha i} \sqrt{M_\alpha}\, r_\alpha \qquad \text{(Equation S4)}$$

Where $K_{\alpha i}$ elements of the Cartesian-normal mode transformation matrix, M_α are the atomic masses. In the LVC model, excited state PESs are created from the reference potential on the basis of state-specific vibronic coupling terms within the W matrix. The diagonal terms of W are given by the following equation:

$$Wxx = \varepsilon_x + \sum_i \kappa_i^{(x)}\, Q_i \qquad \text{(Equation S5)}$$

The off-diagonal terms are given by:

$$Wxy = \sum_i \lambda_i^{(x,y)}\, Q_i. \qquad \text{(Equation S6)}$$

where ε_x are the vertical excitation energies at the reference geometry, while $\kappa_i^{(x)}$ the state-specific gradient at the reference geometry and $\lambda_i^{(x,y)}$ are linear vibronic coupling constant. The low-frequency modes in harmonic oscillators tend to exhibit large nuclear displacements, these displacements are unrealistic, such modes are very often anharmonic, and also very large displacement leads to larger contributions of $\lambda_i^{(x,y)} Q_i$ and this results in a spurious coupling between all states. To avoid this problem, we choose normal modes with ω_i > 300 cm^{-1}.

1.2b SHARC dynamics.[1, 3, 4]

For non-adiabatic dynamics simulation of both DMICE-Br_2 and DMICE-Br_3, A total of 3000 initial conditions were generated by the Wigner distribution of the harmonic oscillator of the ground state. Trajectory surface hopping was carried out by the SHARC method on PESs surface generated by the LVC model, using the PySHARC driver. The nuclear motion is described by integrating Newton second law of equation.

$$M_\alpha \frac{\partial^2 r_\alpha}{\partial t^2} = -\mathrm{g}_m^{diag} \qquad \text{(Equation S7)}$$

Where $-g_m^{diag}$ denotes the negative gradient of the electronic energy of the current active state. The details about the SHARC dynamics are described elaborately in the reference literature. The crossing geometry for S_1-T_2 and T_2-T_1 transitions were obtained by using crossing.py script included in the SHARC 3.0 package.

1.3 Hirshfeld Analysis[5]

The intermolecular interactions within the structure of DMICE-Br_2 and DMICE-Br_3 were recognized through Hirshfeld surface analysis using CrystalExplorer17 software.[6] The Hirshfeld surface is described as the set of points in three-dimensional space where the ratio of the electron densities of the promolecule and procrystal equals to 0.5. Intermolecular interactions are analyzed by mapping normalized contact distances (d_{norm}), which depend on the shortest distance from a point on the surface to the nearest nucleus inside (d_i) and outside (d_e) the surface, as well as the van der Waals radii (r_{vdw}) of the atoms involved. 2D fingerprint plots derived from the Hirshfeld surface analyses, by plotting the fraction of points on the surface as the function of di and de, provide a visual summary of intermolecular contacts within the crystal.

1.4 Noncovalent interaction (NCI) Plot[7]

NCI (Non-Covalent Interaction) analysis utilizes an index derived from electron density and its gradients to identify noncovalent interactions. A two-dimensional plot of reduced density gradient (s) versus electron density (ρ) is used, where the critical points correspond to the troughs observed in the plot, indicating regions of significant noncovalent interactions. Reduced electron density is given by:

$$s = \frac{1}{2(3\pi^2)^{\frac{1}{3}}} \frac{|\nabla\rho|}{\rho^{\frac{4}{3}}} \qquad \text{(Equation S8)}$$

Noncovalent interactions occur in the real space points where these troughs appear. The sign of the second derivative of ρ ($\nabla 2\rho$) is analyzed to distinguish attractive and repulsive interactions. The

noncovalent interaction regions are represented in the plot as discs with colors ranging from green (attractive) to red (repulsive) as in the VIBGYOR spectrum. The wavefunction file generated by Gaussian 16[8] was analyzed using the Multiwfn software[9], and the resulting figures were produced with VMD.

1.5 Symmetry Adapted Perturbation Theory (SAPT)

SAPT(0) analysis was utilized to identify the non-covalent interaction energies of different non-covalent dimers of DMICE-Br_2 and DMICE-Br_3. The SAPT module of the psi4[10] code was employed, with aug-cc-pVDZ basis set. SAPT(0) calculates the interaction energy into its contributing components. The results obtained from the SAPT(0) analysis are a second-order perturbation expansion constituting first-order electrostatic and exchange energy parts, second-order dispersion, induction, and their exchange counterparts as the perturbation terms.

$$E_{int}^{SAPT(0)} = E_{elc}^{(1)} + E_{ex}^{(1)} + E_{ind}^{(2)} + E_{ind-ex}^{(2)} + E_{dis}^{(2)} + E_{dis-ex}^{(2)} \qquad \text{(Equation S9)}$$

1.6 Nanosecond transient absorption (nsTA) measurements

A nanosecond laser flash photolysis experiment was performed on a nitrogen-purged solution of DMICE-Br_2 and DMICE-Br_3 in toluene, by a Photophysics Model LKS-60 laser kinetic spectrometer. The excitation source was a Quanta Ray INDI-40-10 series pulsed Nd: YAG laser, operating at its third harmonic (355 nm, pulse duration≈ 8 ns). The presence of triplet excited states in DMICE-Br_2 and DMICE-Br_3 (O.D. at 355 nm is between 0.1 and 0.2) was confirmed by triplet-triplet energy transfer experiment carried out in toluene solutions of the respective compounds through nanosecond flash photolysis studies.

1.7 Estimation of triplet yields (ϕ_T)[11]

The quantification of the relative triplet yields (ϕ_T) of DMICE-Br_2 and DMICE-Br_3 was measured according to the reported method of energy transfer to beta-carotene by using $[Ru(bpy)_3]Cl_2$ in methanol (ϕ_T≈1) as a reference compound. Optically matched solutions (0.2 to 0.1 OD at 355 nm) of $[Ru(bpy)_3]^{2+}$ in methanol or the solution of DMICE-Br_2 and DMICE-Br_3 in toluene were mixed with a known volume of beta-carotene solution (at millimolar concentration in $CHCl_3$). The decay rate of the triplet excited state in three solutions was measured before the addition of the beta-carotene solution. The transient absorbance (ΔOD) of the beta-carotene triplet, which is populated by energy transfer from $[Ru(bpy)_3]^{2+}$ or the DMICE-Br_2 and DMICE-Br_3 triplet excited state, was monitored at 540 nm. The plateau absorbance, measured after the completion of sensitized triplet formation, was appropriately corrected for the decay of donor triplets competing with energy transfer to beta-carotene. This adjustment allowed for the accurate estimation of the ϕ_T values of the derivatives, based on the following equation.

$$\phi_T^{Sam} = \phi_T^{Ref} \times \frac{\Delta A^{Sam}}{\Delta A^{Ref}} \times \frac{k_{obs}^{Sam}}{k_{obs}^{Sam} - k_0^{Sam}} \times \frac{k_{obs}^{Ref} - k_0^{Ref}}{k_{obs}^{Ref}} \qquad \text{(Equation S9)}$$

where superscripts “Sam” and “Ref” specify the sample DMICE-Br_2/DMICE-Br_3 and reference $[Ru(bpy)_3]Cl_2$, respectively. k_{obs} is the pseudo-first-order rate constant for the growth of the beta-carotene triplet, and k_0 is the rate constant for the decay of the donor triplets (in the absence of beta-carotene) in solutions that contained DMICE-Br_2, DMICE-Br_3 and $[Ru(bpy)_3]Cl_2$ at the same optical density (OD) as the solutions used for sensitization.

1.8 Femtosecond Transient Absorption (fsTA) Measurements

A Spectra-Physics Mai Tai SP mode-locked laser (86 MHz, 800 nm) was used as a seed for a SpectraPhysics Spitfire ace regenerative amplifier (1 kHz, 5.5 mJ). A fraction of the amplified output was used to produce a 325 nm pump pulse by TOPAS. A residual pulse of 800 nm was sent through an optical delay line inside an ExciPro pump-probe spectrometer to produce a white light continuum by employing a sapphire crystal. The white light continuum was split into two, and the streams were used as a probe and reference pulses. The femtosecond transient absorption spectra of the sample were recorded using a dual diode array detector, having a 200 nm detection window and 3.5 ns optical delay. Sample solutions were

prepared in a rotating cuvette with a 1.2 mm path length. Determination of an appropriate instrument response function (IRF) is needed for accurate deconvolution of recorded transient absorption data. The IRF was determined by a solvent (10% benzene in methanol) two-photon absorption and was found to be ~110 fs at about 530 nm. A neutral density filter (80%) was used to control the incident flux on the sample. fsTA measurements of DMICE-Br_2 and DMICE-Br_3 in toluene were recorded by photoexciting the sample with 325 nm, 200 nJ, and 100 fs pulses. The observed kinetic components were laser intensity-independent. The intersystem crossing rate was calculated by taking the inverse of the singlet lifetime ($k_{ISC} = \frac{1}{\tau}$), Where τ is the lifetime of singlet decay obtained in fsTA measurement.

1.9 Global Analysis[12]

Global analyses of the fsTA spectra were performed using the Glotaran software. The procedure evaluates the instrument time response function and the group velocity dispersion of the white continuum and allowsone to compute decay time constants and dispersion-compensated spectra. All the wavelengths were analyzed in global analyses concurrently, employing a sequential model to give evolution-associated spectra (EAS). The EAS indicates the spectral changes that occur with the associated time constants and does not necessarily denote a real physical/chemical species. analyzed in global analyses concurrently, employing a sequential model to give evolution-associated spectra (EAS). The EAS indicates the spectral changes that occur with the associated time constants and does not necessarily denote a real physical/chemical species.

Section B: Synthesis and Characterization[13]

Synthesis:

2.1 DMICE-Br_2: To a 50 mL round bottom flask added ethyl 5,6-dimethoxyindole-2-carboxylate, DMICE (1 equiv, 0.50 mmol) and NBS (4.0 equiv, 2.0 mmol). Then 10 mL of THF were added into 50 mL round bottom flask and stirred at 65 °C for 2 h, then concentrated in vacuo. The crude product was dissolved in dichloromethane, washed with water, dried over $MgSO_4$, concentrated, and purified by column chromatography (silica, 8:1 hexane/EtOAc) to afford DMICE-Br_2 as a white solid with a 71% yield.

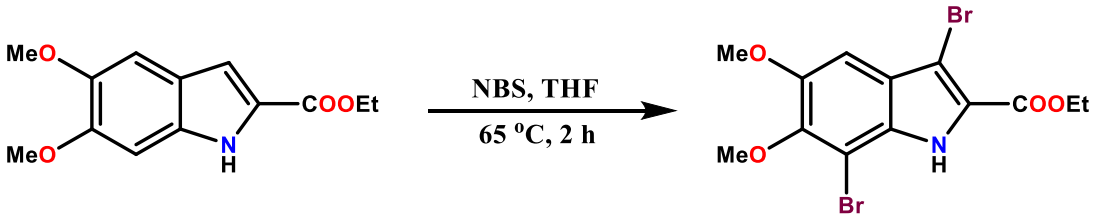

Scheme S1: The reaction scheme for the synthesis of DMICE-Br_2.

2.2 DMICE-Br_3: To a 25-mL round bottom flask added ethyl 5,6-dimethoxyindole-2-carboxylate, DMICE (1 equiv, 0.80 mmol) and NBS (4.0 equiv, 3.2 mmol) and dissolved in 8 mL acetonitrile. The reaction mixture was stirred at 65 °C for 24 hours, then concentrated under reduced pressure. The crude product was dissolved in dichloromethane, washed with water, dried over $MgSO_4$, concentrated, and purified by column chromatography (silica, 3:2 DCM/hexane) to afford DMICE-Br_3 as a white solid with a 10% yield.

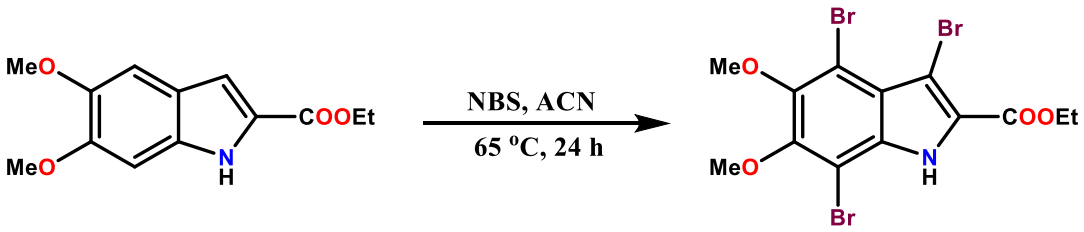

Scheme S1: The reaction scheme for the synthesis of DMICE-Br_3.

Characterization:

a) DMICE-Br_2: ^{1}H NMR (500 MHz, $CDCl_3$, ppm) δ = 8.93 (s, 1H), 7.00 (s, 1H), 4.47 (q, J = 7.1 Hz, 2H), 3.96 (s, 3H), 3.92 (s, 3H), 1.46 (t, J = 7.2 Hz, 3H).
^{13}C NMR (125 MHz, $CDCl_3$, ppm): δ 160.4, 150.4, 147.6, 129.3, 124.5, 123.7, 101.2, 101.1, 98.2, 61.5, 61.2, 56.4, 14.4.
HRMS (APCI) (m/z): Calculated for $C_{13}H_{14}Br_2NO_4$ $[M+H]^+$: 405.9289, found: 405.9115 $[M+H]^+$
Melting Point (°C): 127.5

b) DMICE-Br_3: ^{1}H NMR (500 MHz, $CDCl_3$, ppm) δ 9.00 (s, 1H), 4.41 (q, J = 7.1 Hz, 2H), 3.90 (s, 3H), 3.83 (s, 3H), 1.39 (t, J = 7.1 Hz, 3H).
^{13}C NMR (125 MHz, $CDCl_3$, ppm): δ 159.1, 149.7, 146.7, 130.8, 125.2, 119.5, 109.2, 98.0, 97.5, 60.8, 60.6, 60.1, 13.3.
HRMS (APCI) (m/z): Calculated for $C_{13}H_{13}Br_3NO_4$ $[M+H]^+$: 483.8395, found: 483.8225 $[M+H]^+$
Melting Point (°C): 146.6

Section C: Tables

Table S1: Crystallographic data and refinement parameters for DMICE-Br_2 and DMICE-Br_3.

PARAMETERS	DMICE-Br_2	DMICE-Br_3
Formula	$C_{13}H_{13}Br_2NO_4$	$C_{13}H_{12}Br_3NO_4$
Formula weight	407.04	485.94
Colour	Colorless	Colorless
Crystal system	Monoclinic	Monoclinic
Space group, Z	P 2_1/c, 4	C 2/c, 8
A (Å)	4.33(2)	20.39(4)
B (Å)	13.76(6)	12.62(2)
C (Å)	25.01(12)	14.92(3)
A (deg)	90.00	90
B (deg)	91.81(6)	125.05(5)
Γ (deg)	90.00	90
Volume, A^3	1490.6(12)	3143.0(10)
R-factor	5.44	4.18
Temp (K)	296	296
$Density_{calc}$(Mg/m^3)	1.81	2.05
No. of reflections collected	20764	3091
Independent reflections	3752	3091
$2\Theta_{MAX}$ (deg)	57.0	52.0
R indices, wR2, (i>2s(i))	0.054	0.042
R indices, wR2 (all data)	0.102	0.095
Goodness of fit	1.030	0.980
CCDC number	2387375	2387376

Table S2: Relative % intermolecular interactions obtained from Hirshfeld analysis.

	DMICE-Br_2	DMICE-Br_3
Br•••H	23.3	30.5
H•••H	35.6	29.7
O•••H	16.8	15.5
C•••C	4.9	7.6
Br•••Br	0.7	4.5
C•••Br	2.8	3.5
N•••C	1.2	1.7
N•••N	0	0.3
C•••O	3	1.8
Br•••O	2.9	1.3
N•••Br	0	0.1
C•••H	7.9	2.7

Table S3: Interaction energies (in kJ/mol) of DMICE-Br_2 dimers evaluated using symmetry-adapted perturbation theory (SAPT(0)) aug-cc-pVDZ calculations.

Dimer	Electrostatic	Exchange	Induction	Dispersion	Total SAPT(0)
Dimer-1	-5.008	12.582	-1.373	-24.473	**-18.272**
Dimer-2	-6.707	9.715	-2.018	-9.518	**-8.528**
Dimer-3	-1.726	3.604	-0.534	-7.920	**-6.577**
Dimer-4	-1.471	2.449	-0.356	-3.625	**-3.003**

Table S4: Interaction energies (in kJ/mol) of DMICE-Br_3 dimers evaluated using symmetry-adapted perturbation theory (SAPT(0)) aug-cc-pVDZ calculations.

Dimer	Electrostatic	Exchange	Induction	Dispersion	Total SAPT(0)
Dimer-1	-9.608	15.026	-1.921	-30.199	**-26.704**
Dimer-2	-12.487	18.792	-3.069	-33.489	**-30.253**
Dimer-3	-1.395	2.979	-0.438	-3.724	**-2.578**
Dimer-4	-1.791	4.632	-0.329	-4.369	**-1.857**

Table S5: Singlet-triplet energy gaps and spin-orbit coupling matrix elements for DMICE-Br_2 and DMICE-Br_3 calculated at the reference geometries using SHARC-ORCA.

Compounds	Singlet	Triplet	SOC (cm^{-1})	ΔE_{ST} (eV)
DMICE-Br_2	S_1	T_1	0.91	0.96
	S_1	T_2	0.53	0.68
	S_1	T_3	0.68	-0.25
DMICE-Br_3	S_1	T_1	1.56	1.06
	S_1	T_2	1.31	0.38
	S_1	T_3	6.13	-0.17

Table S6: Vertical excitation energies of the singlet and triplet excited states (calculated at B3LYP/def2-tzvp level of theory) of DMICE-Br_2.

Singlet	Energy (eV)	f	Triplet	Energy (eV)	f
S_1	3.71	0.15	T_1	2.75	0
S_2	4.12	0.73	T_2	3.03	0
S_3	4.72	0.00	T_3	3.96	0
S_4	4.81	0.00	T_4	4.35	0
S_5	4.89	0.00	T_5	4.41	0
S_6	4.97	0.00	T_6	4.61	0
S_7	5.14	0.00	T_7	4.74	0
S_8	5.26	0.04	T_8	4.75	0
S_9	5.30	0.05	T_9	4.82	0
			T_{10}	4.86	0

Table S7: Vertical excitation energies of the singlet and triplet excited states (calculated at B3LYP/def2- tzvp level of theory) of DMICE-Br_3.

Singlet	Energy (eV)	f	Triplet	Energy (eV)	f
S_1	3.79	0.24	T_1	2.73	0
S_2	4.28	0.50	T_2	3.41	0
S_3	4.42	0.00	T_3	3.96	0
S_4	4.59	0.00	T_4	4.24	0
S_5	4.75	0.02	T_5	4.30	0
S_6	4.97	0.00	T_6	4.38	0
S_7	5.02	0.00	T_7	4.65	0
S_8	5.12	0.00	T_8	4.69	0
S_9	5.15	0.00	T_9	4.82	0
			T_{10}	4.83	0

Table S8: Time constants obtained by fitting a sequential first-order kinetics model to the population data for both DMICE-Br_2 and DMICE-Br_3.

Process	Time constant (ps) (DMICE-Br_2)	Time constant (ps) (DMICE-Br_3)
$S_1 \rightarrow T_{2,3}$	28.95	3.15
$T_{2,3} \rightarrow T_1$	24.78	0.55
$S_1 \rightarrow T_1$	38.54	3.43
$S \rightarrow T$	21.14	2.42

Section D: Figures

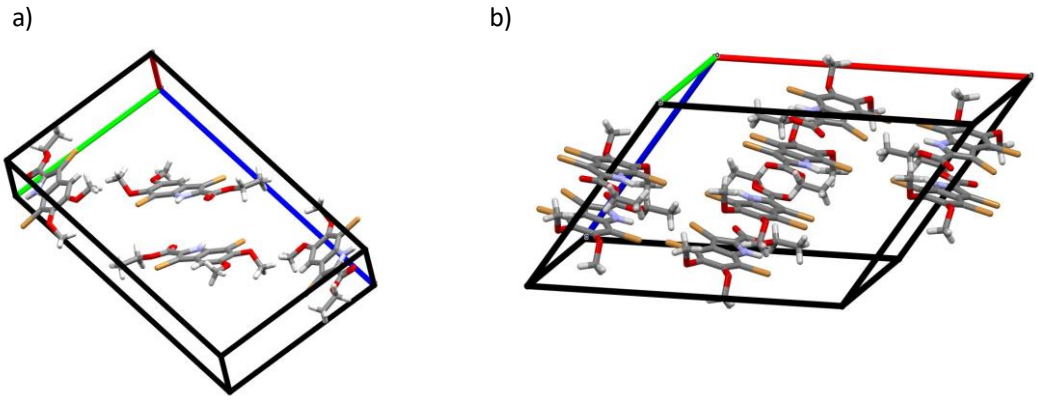

Figure S1: Unit cell packing in a) DMICE-Br_2 and b) DMICE-Br_3

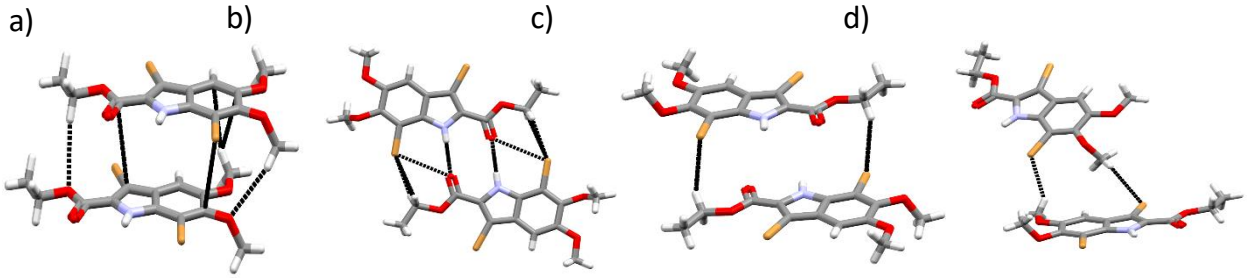

Figure S2: Identified dimers of DMICE-Br_2: a) DMICE-Br_2-D1, b) DMICE-Br_2-D2, c) DMICE-Br_2-D3 and d) DMICE-Br_2-D4.

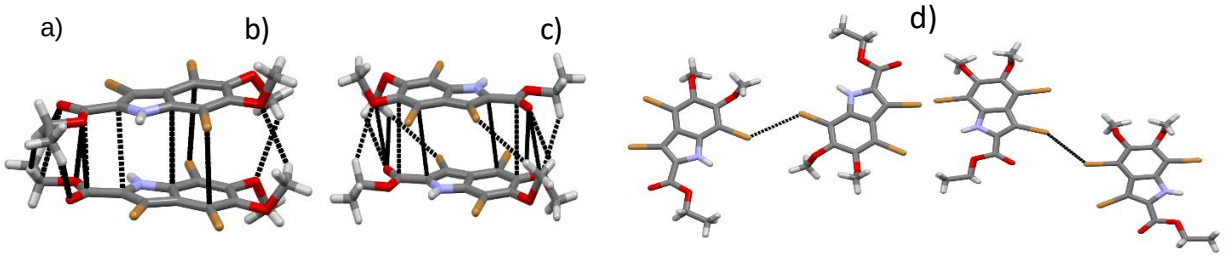

Figure S3: Identified dimers of DMICE-Br_3: a) DMICE-Br_3-D1, b) DMICE-Br_3-D2 and c) DMICE-Br_3-D3 and d) DMICE-Br_3-D4.

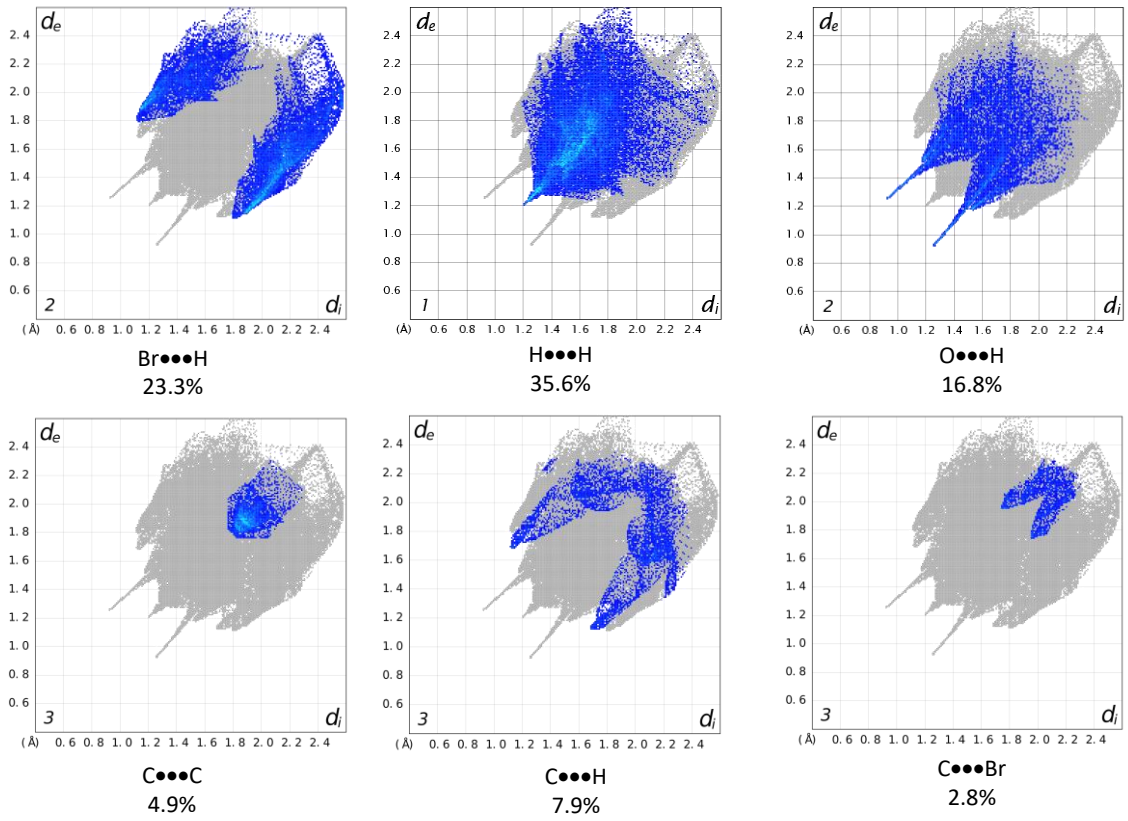

Figure S4: Hirshfeld Surface Analysis of DMICE-Br_2.

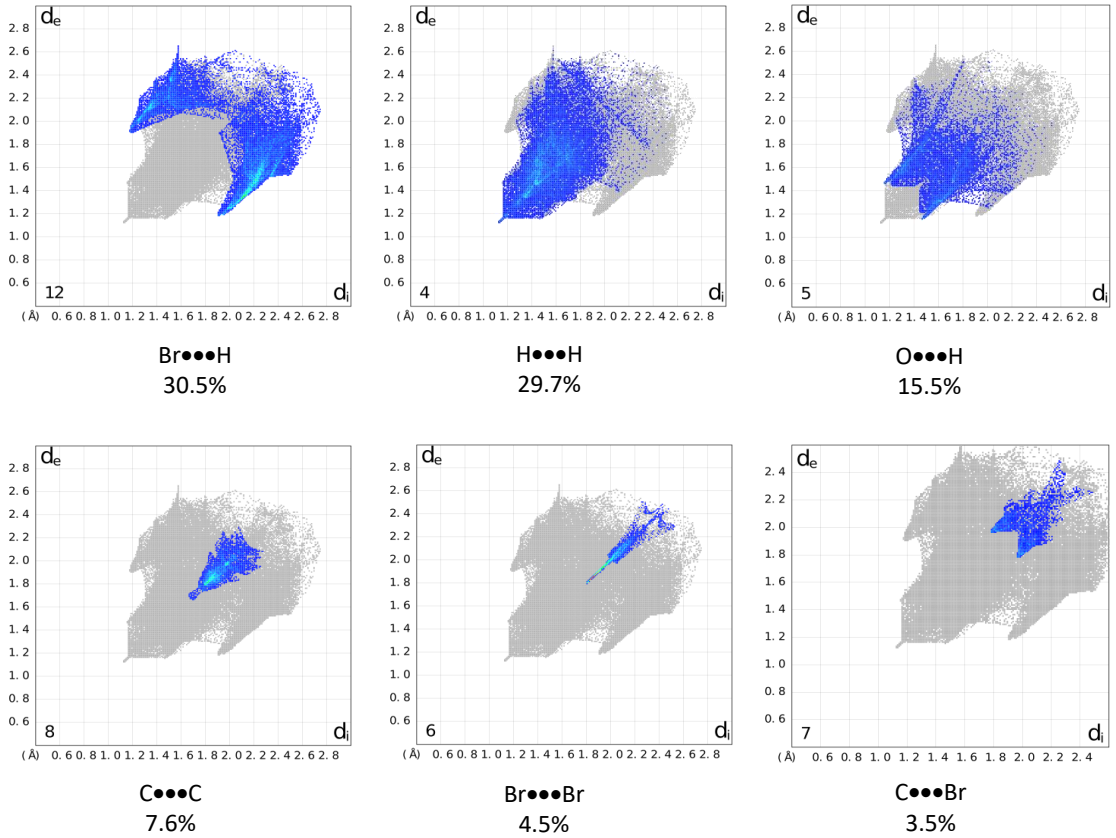

Figure S5: Hirshfeld Surface Analysis of DMICE-Br_3.

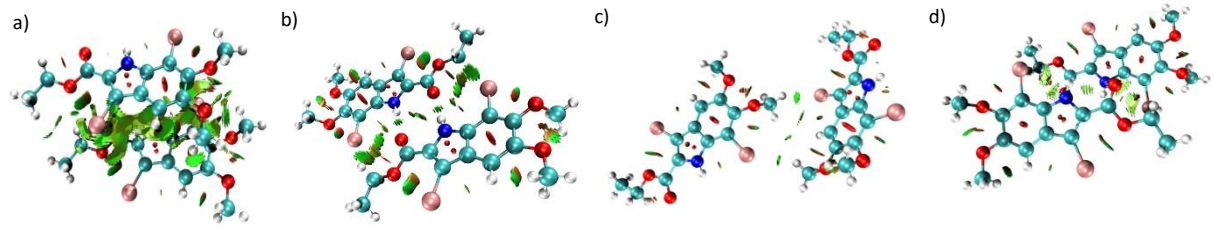

Figure S6: NCI plot showing identified DMICE-Br_2 dimers (a) DMICE-Br_2-D1, (b) DMICE-Br_2-D2, (c) DMICE Br_2-D3, and (d) DMICE-Br_2-D4, with weak stabilizing interactions represented as green disks.

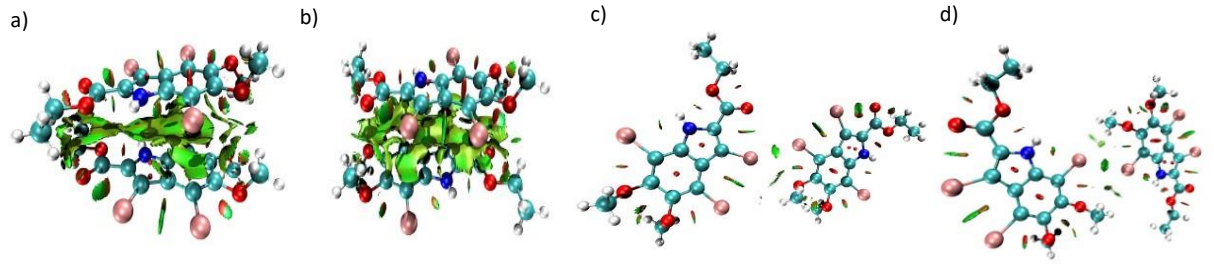

Figure S7: NCI plot showing identified DMICE-Br_3 dimers (a) DMICE-Br_3-D1, (b) DMICE-Br_3-D2, (c) DMICE-Br_3-D3, and (d) DMICE-Br_3-D4, with weak stabilizing interactions represented as green disks.

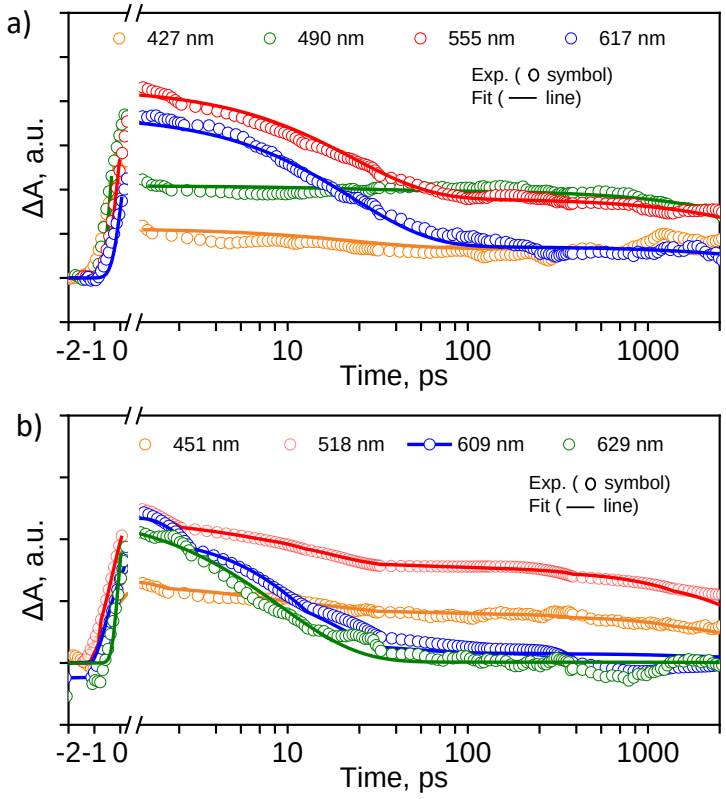

Figure S8: Overlay of experimental traces (symbol) and fitted traces (line) at different wavelengths for a) DMICE-Br_2 and b) DMICE-Br_3.

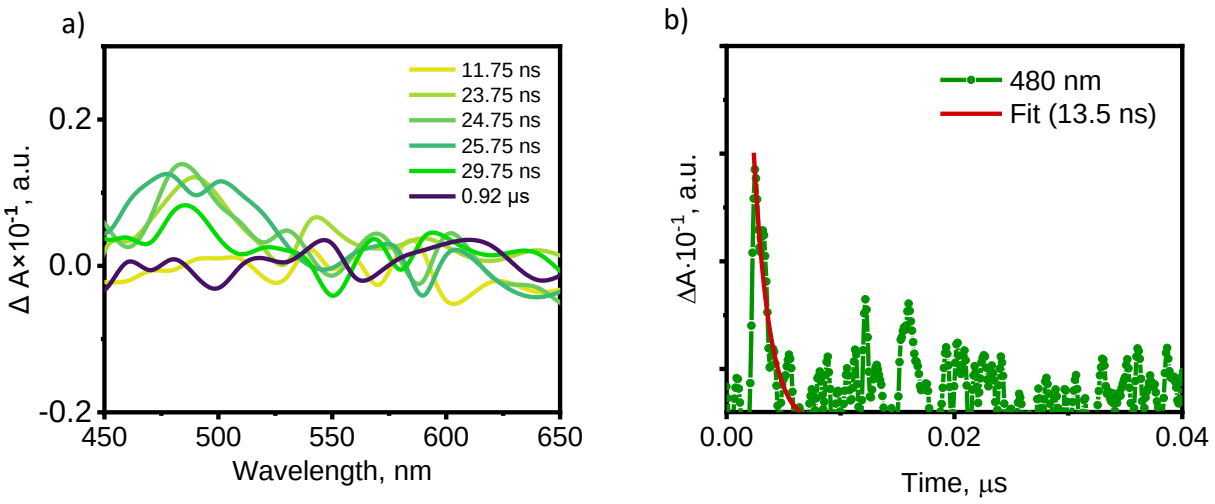

Figure S9: a) Nanosecond transient absorption traces at different time delays for DMICE-Br_2 in de-aerated toluene; b) Decay kinetics at 480 nm depicting the difference in triplet lifetimes for DMICE-Br_2.

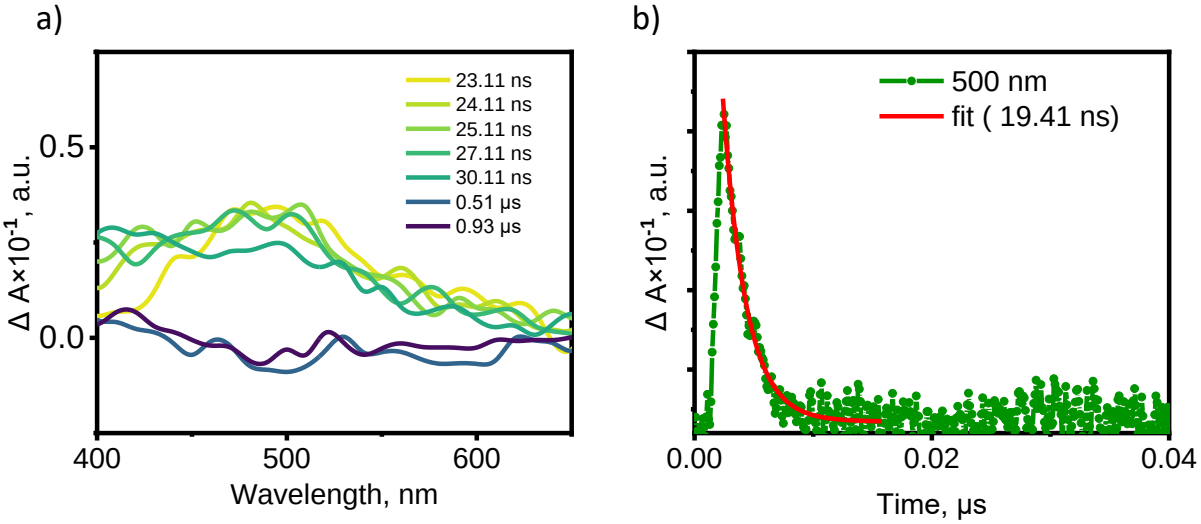

Figure S10: a) Nanosecond transient absorption traces at different time delays for DMICE-Br_3 in de-aerated toluene; b) Decay kinetics at 500 nm depicting the difference in triplet lifetimes for DMICE-Br_3.

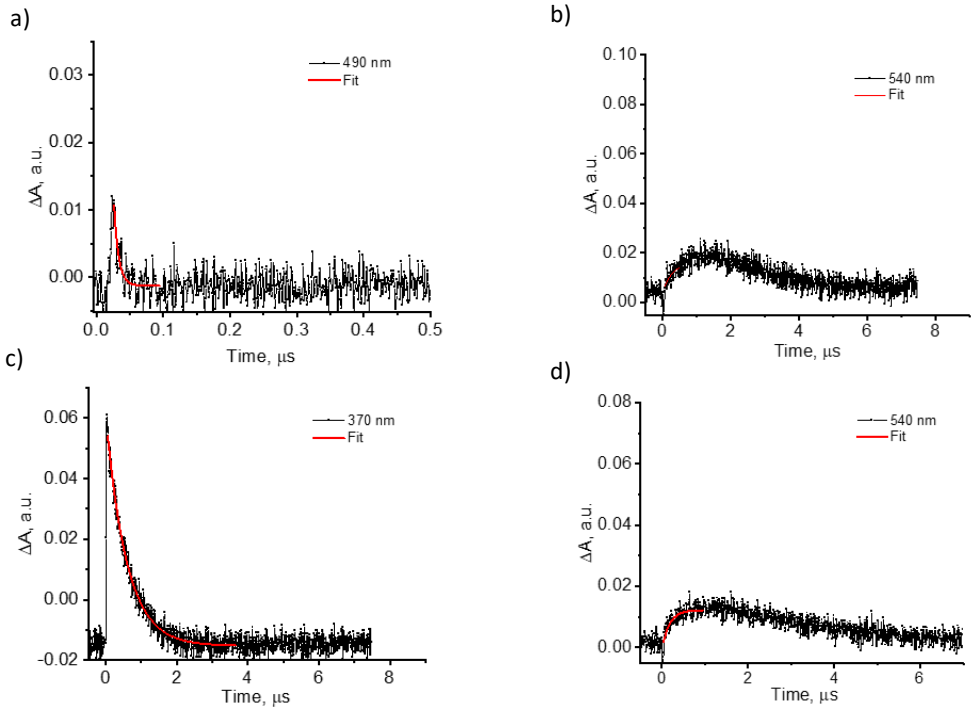

Figure S11: Triplet-triplet energy transfer experiments for DMICE-Br_2. Nanosecond transient absorption traces at 355 nm excitation a) before addition of β-carotene in N_2-purged toluene for DMICE-Br_2, b) after addition of β-carotene in N_2-purged toluene for DMICE-Br_2, c) before addition of β-carotene in N_2-purged methanol for $[Ru(bpy)_3]Cl_2$ d) after addition of β-carotene in N_2-purged methanol for $[Ru(bpy)_3]Cl_2$.

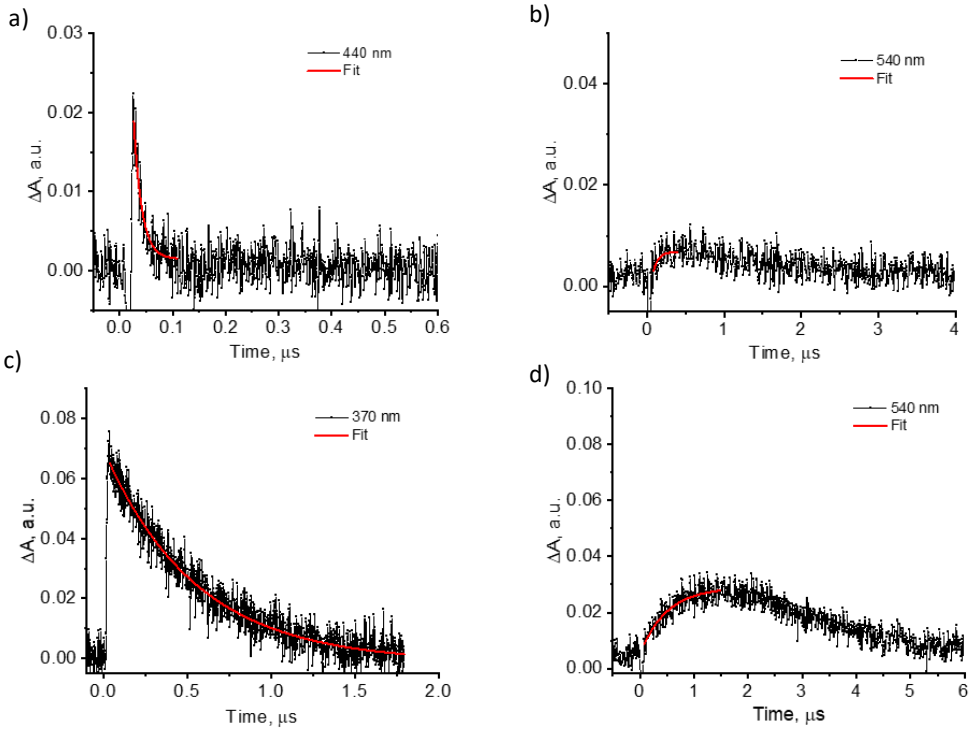

Figure S12: Triplet-triplet energy transfer experiments for DMICE-Br_3. Nanosecond transient absorption traces at 355 nm excitation a) before addition of β-carotene in N_2-purged toluene for DMICE-Br_3, b) after addition of β-carotene in N_2-purged toluene for DMICE-Br_3, c) before addition of β-carotene in N_2-purged methanol for $[Ru(bpy)_3]Cl_2$ d) after addition of β-carotene in N_2-purged methanol for $[Ru(bpy)_3]Cl_2$.

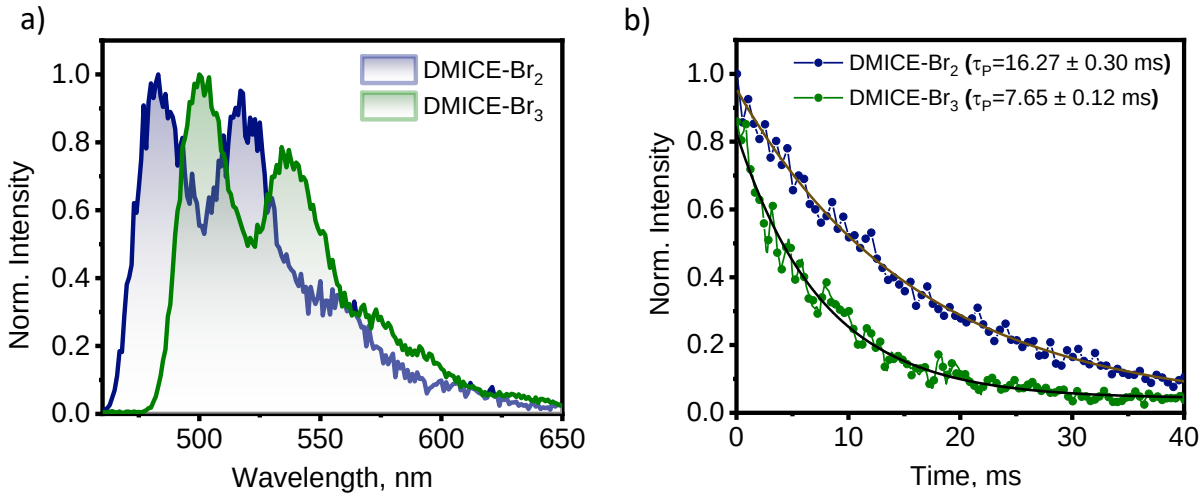

Figure S13: a) Delayed emission spectra of DMICE-Br_2 and DMICE-Br_3 at 77 K (in liquid N_2) in toluene a delay of 0.05 ms at λ_{exc}=340 nm, b) Decay time plot of the delayed emission of DMICE-Br_2 and DMICE-Br_3 at 485 nm and 500 nm at 77 K (in liquid N_2) in toluene. The measurements were performed at a delay of 0.05 ms (Time per flash=80 ms) at λ_{exc}=340 nm.

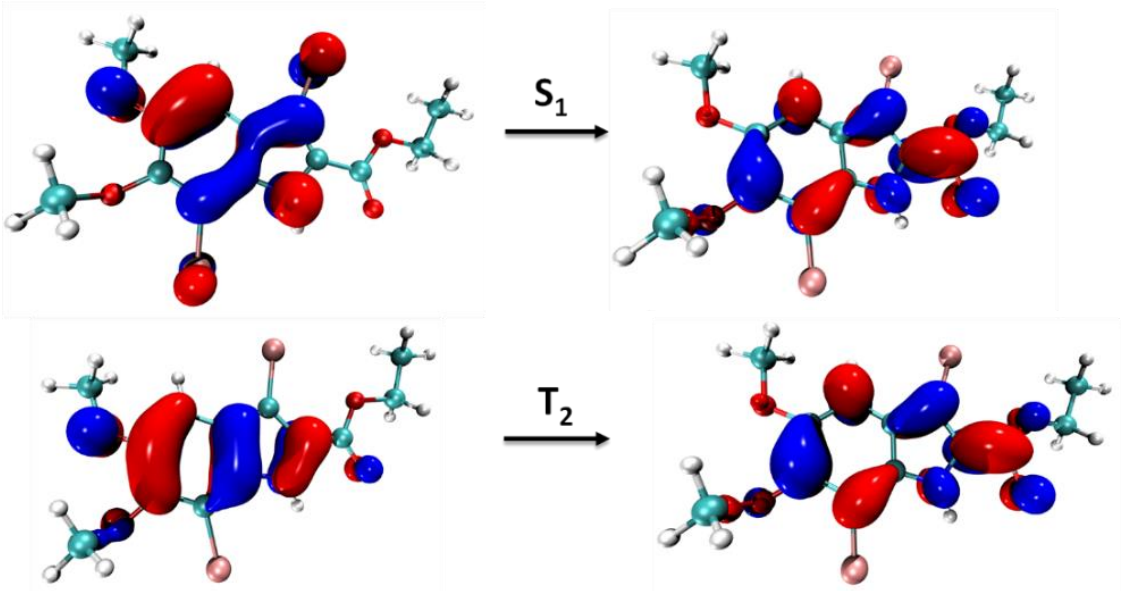

Figure S14: Natural Transition Orbitals (NTOs) for the S_1 and T_2 states of DMICE-Br_2 calculated at the B3LYP/def2-tzvp level of theory (iso-value = 0.04 e-bohr^{-3}).

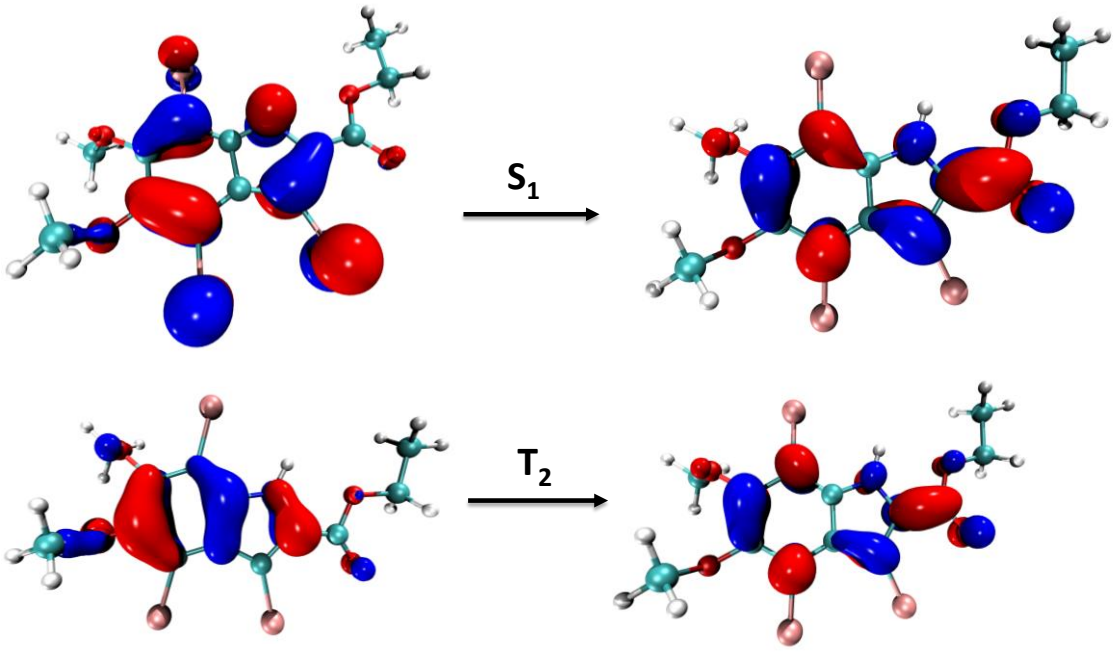

Figure S15: Natural Transition Orbitals (NTOs) for the S_1 and T_2 states of DMICE-Br_3 calculated at the B3LYP/def2-tzvp level of theory (iso-value = 0.04 e-bohr^{-3}).

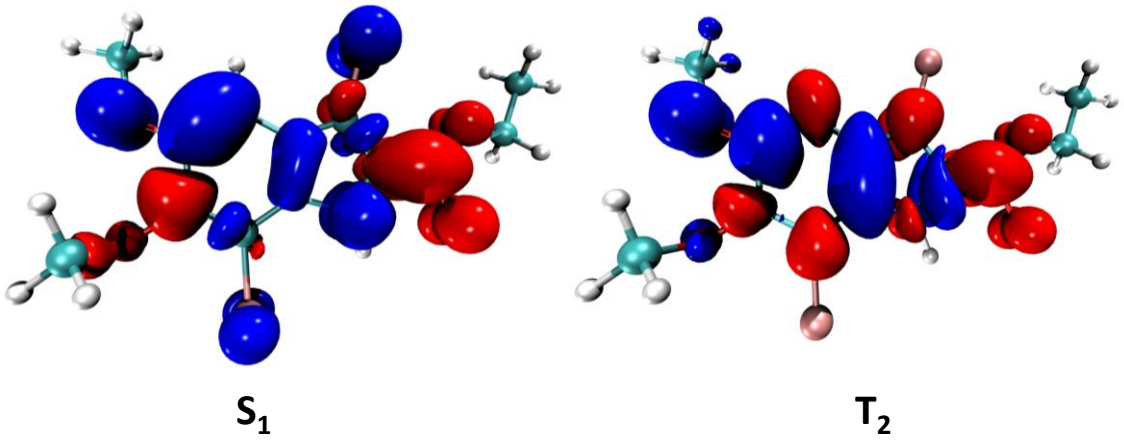

Figure S16: Charge density difference plot for the S_1 and T_2 states of DMICE-Br_2 calculated at the B3LYP/def2-tzvp level of theory. Blue denotes electron and red denotes hole densities (iso-value = 0.001 e-bohr^{-3}).

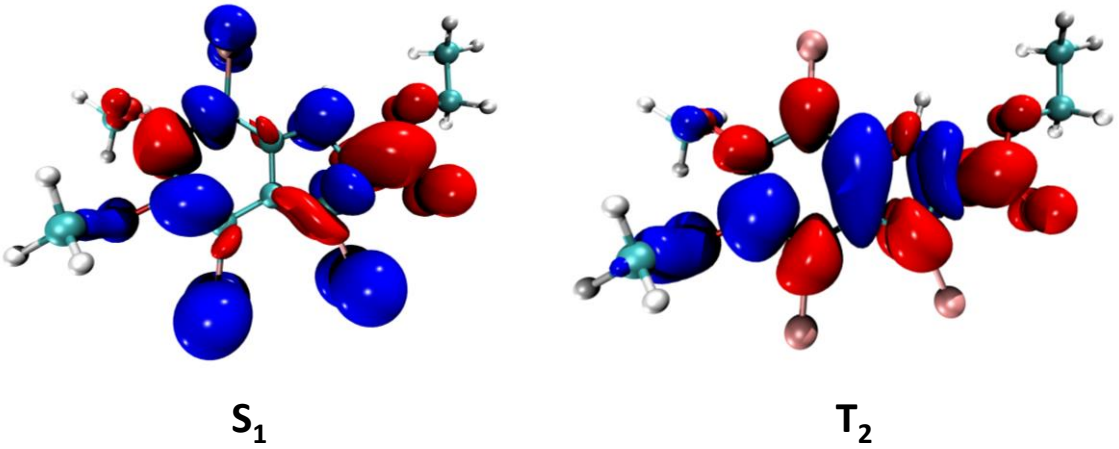

Figure S17: Charge density difference plot for the S_1 and T_2 states of DMICE-Br_3 calculated at the B3LYP/def2-tzvp level of theory. Blue denotes electron and red denotes hole densities (iso-value = 0.001 e-bohr^{-3}).

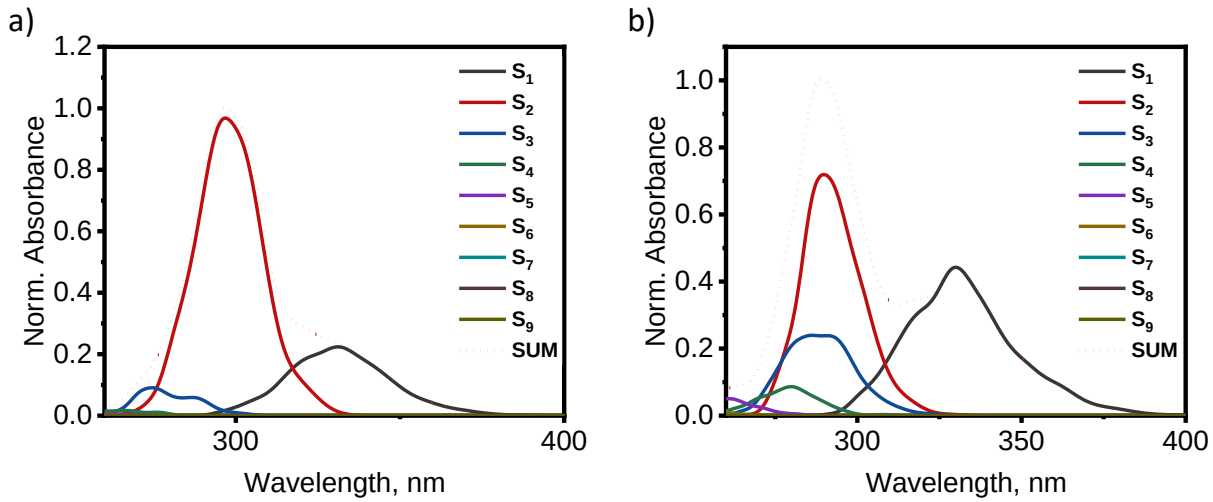

Figure S18: Computed absorption spectrum of a) DMICE-Br_2 and b) DMICE-Br_3

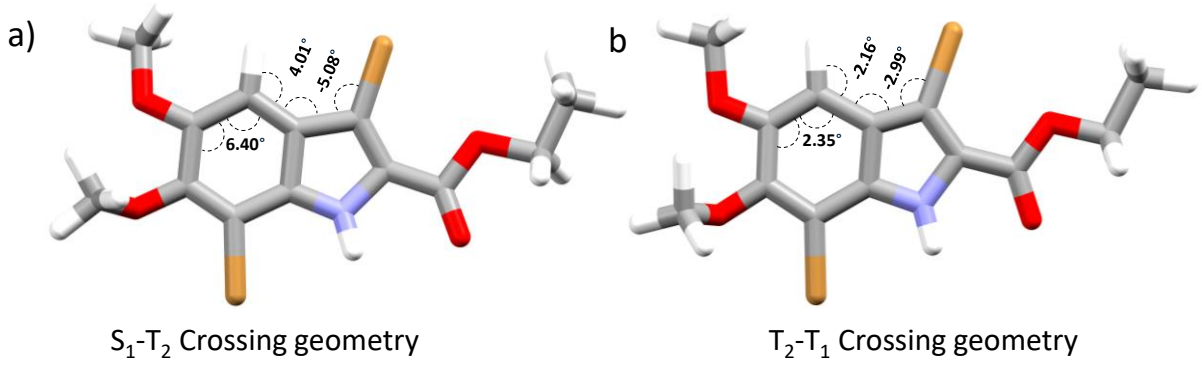

Figure S19: a) S_1-T_2 and b) T_2-T_1 crossing geometries for DMICE-Br_2.

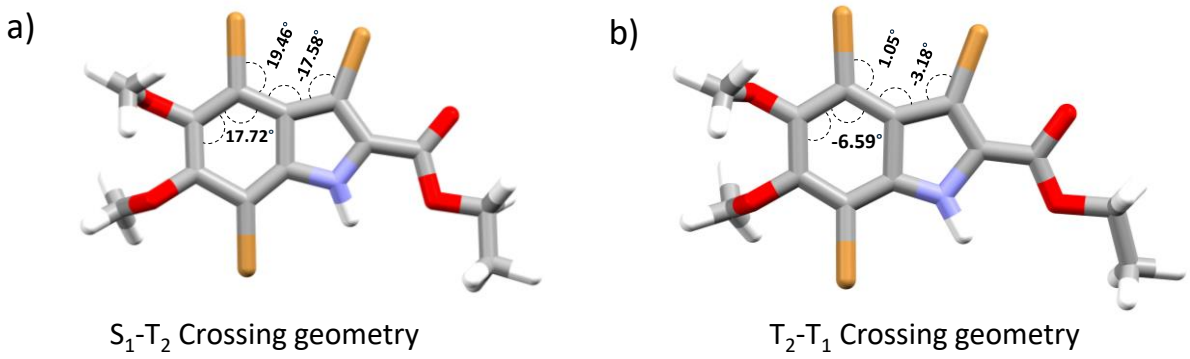

Figure S20: a) S_1-T_2 and b) T_2-T_1 crossing geometries for DMICE-Br_3.

Section E: Appendix – Characterization Data

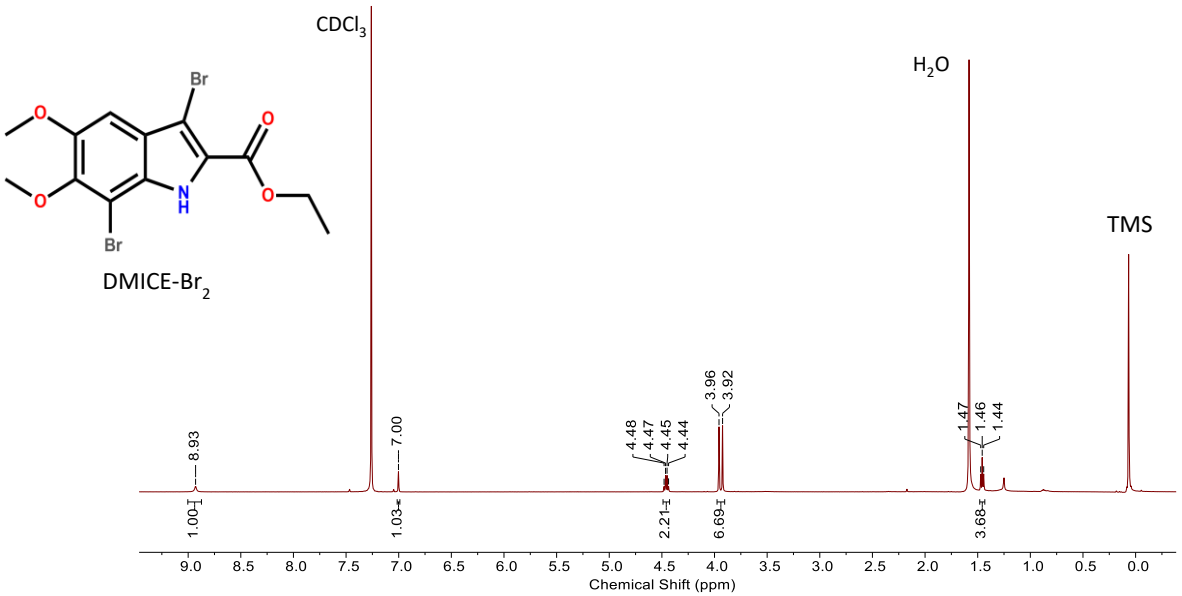

Figure A1: ^{1}H-NMR of DMICE-Br_2 in $CDCl_3$.

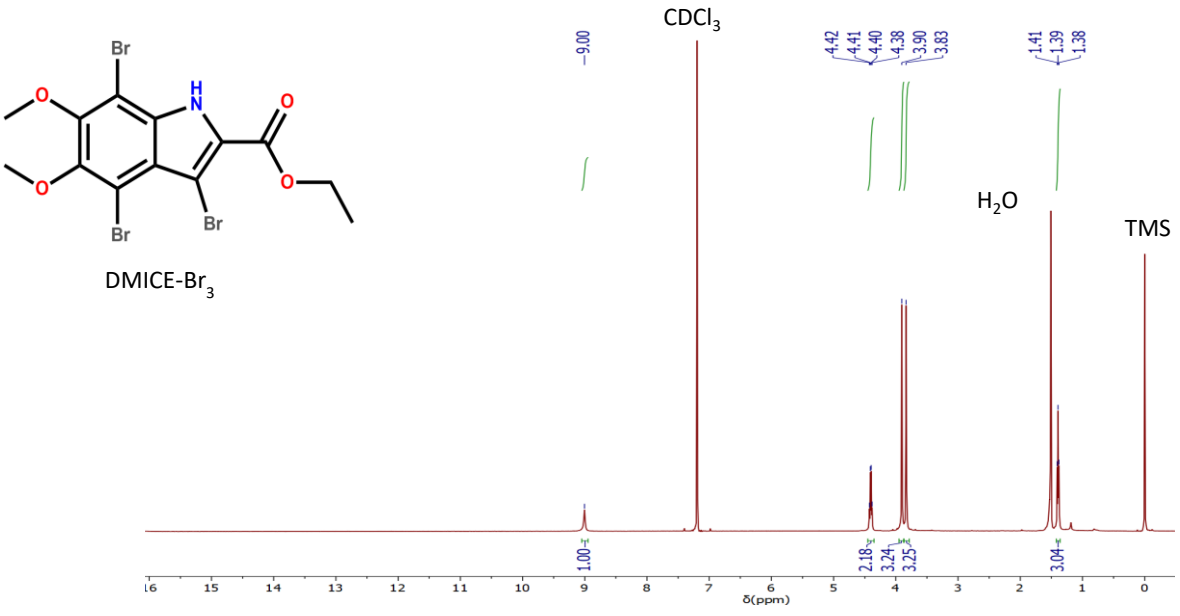

Figure A2: ^{1}H-NMR of DMICE-Br_3 in $CDCl_3$.

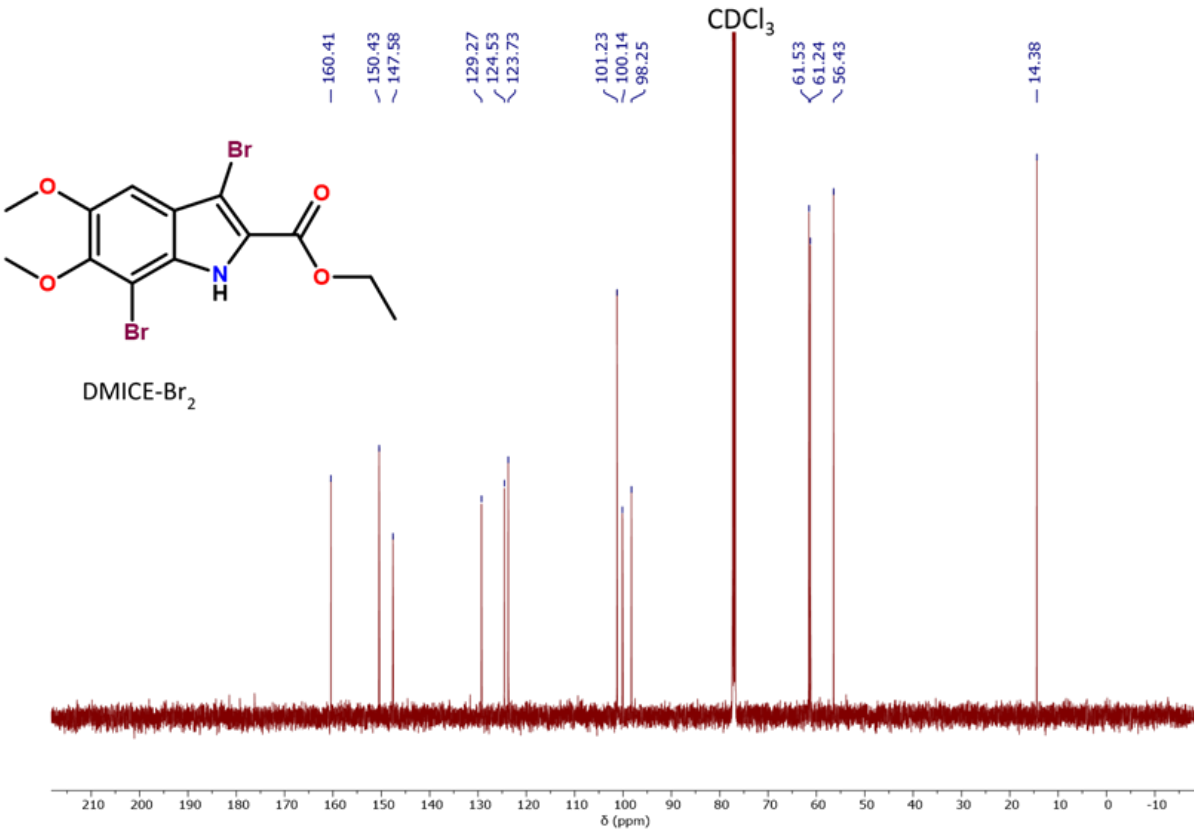

Figure A4: ^{13}C-NMR of DMICE-Br_2 in $CDCl_3$.

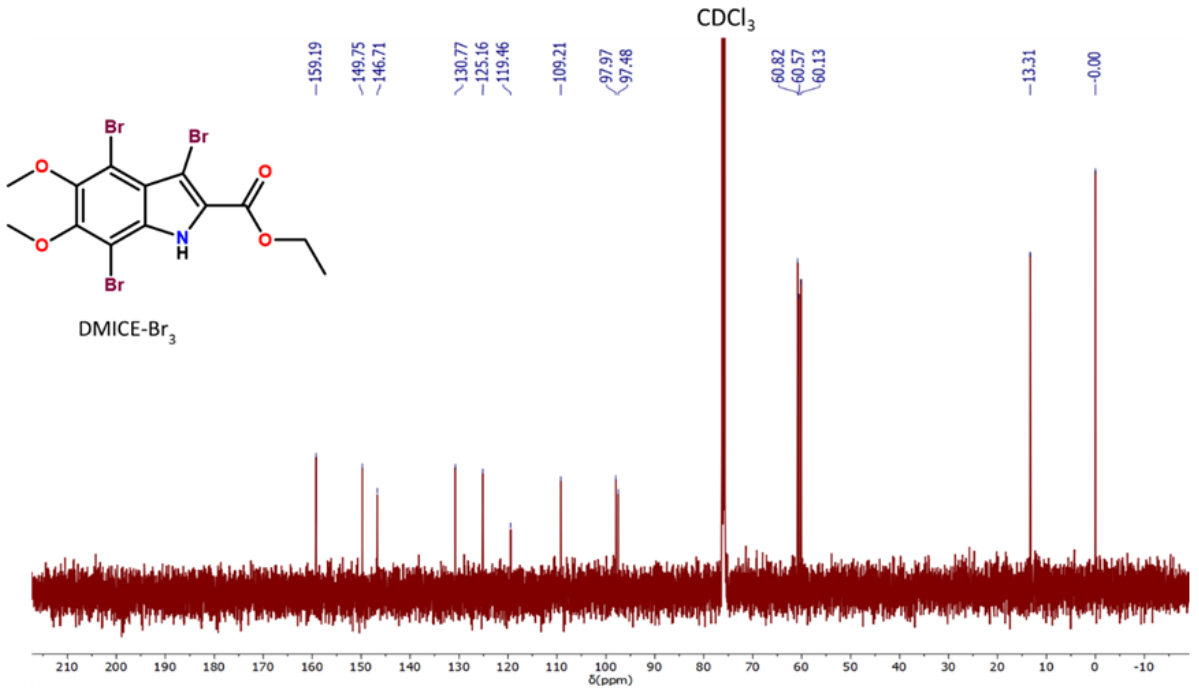

Figure A5: ^{13}C-NMR of DMICE-Br_3 in $CDCl_3$.

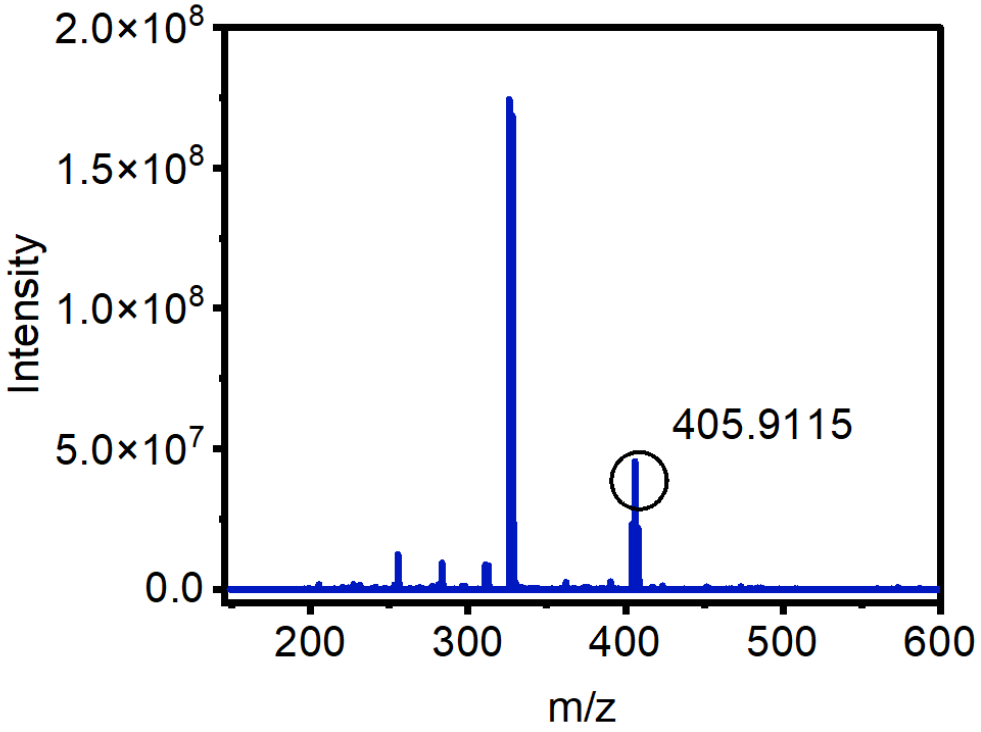

Figure A5: HRMS spectrum of DMICE-Br_2.

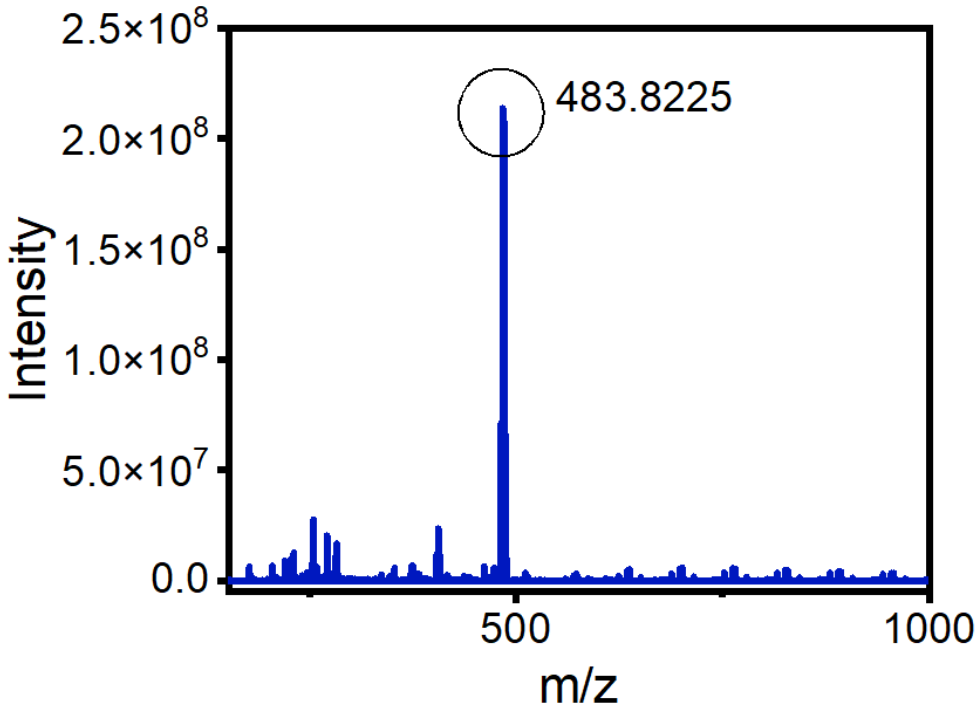

Figure A6: HRMS spectrum of DMICE-Br_3.

References

1. F. Plasser, S. Gómez, M. F. S. J. Menger, S. Mai and L. González, *Phys. Chem. Chem. Phys.*, 2019, **21**, 57-69.
2. S. Mai, M. Menger, M. Marazzi, D. L. Stolba, A. Monari and L. González, *Theor. Chem. Acc*, 2020, **139**, 65.
3. S. Mai, P. Marquetand and L. González, *Wiley Interdiscip. Rev. Comput. Mol. Sci.*, 2018, **8**, e1370.
4. S. Mai, P. Marquetand and L. González, in *Quantum Chemistry and Dynamics of Excited States*, 2020, pp. 499-530.
5. M. A. Spackman and D. Jayatilaka, *CrystEngComm*, 2009, **11**, 19-32.
6. P. R. Spackman, M. J. Turner, J. J. McKinnon, S. K. Wolff, D. J. Grimwood, D. Jayatilaka and M. A. Spackman, *J. Appl. Crystallogr.*, 2021, **54**, 1006-1011.
7. J. Contreras-García, E. R. Johnson, S. Keinan, R. Chaudret, J.-P. Piquemal, D. N. Beratan and W. Yang, *J. Chem. Theory Comput.*, 2011, **7**, 625-632.
8. G. W. T. M. J. Frisch, H. B. Schlegel, G. E. Scuseria, M. A. Robb, J. R. Cheeseman, G. Scalmani, V. Barone, G. A. Petersson, H. Nakatsuji, X. Li, M. Caricato, A. V. Marenich, J. Bloino, B. G. Janesko, R. Gomperts, B. Mennucci, H. P. Hratchian, J. V. Ortiz, A. F. Izmaylov, J. L. Sonnenberg, D. Williams-Young, F. Ding, F. Lipparini, F. Egidi, J. Goings, B. Peng, A. Petrone, T. Henderson, D. Ranasinghe, V. G. Zakrzewski, J. Gao, N. Rega, G. Zheng, W. Liang, M. Hada, M. Ehara, K. Toyota, R. Fukuda, J. Hasegawa, M. Ishida, T. Nakajima, Y. Honda, O. Kitao, H. Nakai, T. Vreven, K. Throssell, J. A. Montgomery Jr., J. E. Peralta, F. Ogliaro, M. J. Bearpark, J. J. Heyd, E. N. Brothers, K. N. Kudin, V. N. Staroverov, T. A. Keith, R. Kobayashi, J. Normand, K. Raghavachari, A. P. Rendell, J. C. Burant, S. S. Iyengar, J. Tomasi, M. Cossi, J. M. Millam, M. Klene, C. Adamo, R. Cammi, J. W. Ochterski, R. L. Martin, K. Morokuma, O. Farkas, J. B. Foresman, D. J. Fox, *Gaussian 16, Revision C.01, Gaussian, Inc., Wallingford CT 2016.*
9. T. Lu and F. Chen, *J. Comput. Chem.*, 2012, **33**, 580-592.
10. S. Ito, T. Nagami and M. Nakano, *Phys. Chem. Chem. Phys.*, 2017, **19**, 5737-5745.
11. A. Mohan, E. Sebastian, M. Gudem and M. Hariharan, *J. Phys. Chem. B.*, 2020, **124**, 6867-6874.
12. J. J. Snellenburg, S. Laptenok, R. Seger, K. M. Mullen and I. H. M. van Stokkum, *J. Stat. Softw.*, 2012, **49**, 1 - 22.
13. A. H. Aebly, Jeffrey N. Levy, B. J. Steger, J. C. Quirke and J. M. Belitsky, *RSC Adv.*, 2018, **8**, 28323-28328.